KeAi
CHINESE ROOTS
GLOBAL IMPACT

Available online at www.sciencedirect.com

ScienceDirect

Green Energy & Environment 11 (2026) 1324−1334

www.keaipublishing.com/gee

Research Paper

Transferable molecular model for benzimidazole-linked polymer membranes applied in hydrogen separation

Qianqian Zhu [a], Shaofan Duan [a], Meixia Shan [a,*], Freek Kapteijn [b], Xin Gao [c], Yatao Zhang [a], Dongyang Li [a,*]

[a] School of Chemical Engineering, Zhengzhou University, Zhengzhou, 450002, China
[b] Chemical Engineering Department, Delft University of Technology, Van der Maasweg 9, HZ Delft, 2629, the Netherlands
[c] School of Chemical Engineering and Technology, National Engineering Research Center of Distillation Technology, Tianjin University, Tianjin, 300072, China

Received 1 September 2025; revised 14 December 2025; accepted 30 December 2025
Available online 10 January 2026

Abstract

Benzimidazole-linked polymers (BILPs), with their densely cross-linked ultramicroporous networks, are promising for hydrogen separation. However, the molecular selectivity mechanisms remain poorly understood, hindering rational design. We present a multiscale simulation for BILPs, using BILP-101 as a model, to precisely resolve its microstructural features and elucidate H_2 separation performance at an unprecedented molecular level. Through meticulous optimization of simulation protocols, including force fields, atomic charges, chain configurations, and equilibration cycles, optimal simulation protocols were identified, and the interplay of pore architecture and chemical interactions driving H_2 selectivity was uncovered. Our simulations not only demonstrate precise control over pore geometry but also accurately replicate experimental H_2/CO_2, H_2/N_2, H_2/CH_4 separation performance across standard and elevated temperatures. The generality of our model was further validated by its strong agreement with empirical data for BILP-5 and BILP-15. This work bridges advanced molecular modeling with experimental validation, providing design principles to accelerate the development of next-generation BILPs or other polymer membranes for energy-efficient gas separation.

Keywords: Hydrogen separation; Benzimidazole polymer; Molecular simulation; Mechanism explanation

1. Introduction

With the escalating impacts of global warming and the finite nature of fossil fuel reserves, there is an urgent imperative to develop sustainable energy carriers [1]. Hydrogen has emerged as a premier candidate owing to its high gravimetric energy density, renewability, and zero-emission combustion profile [2]. However, the prevailing industrial route inevitably generates substantial CO_2 [3]. Among the principal purification techniques, membrane technology stands out for its low energy demand, operational simplicity, and compact footprint [4,5]. To date, only polymeric membranes have demonstrated industrial viability for H_2/CO_2 separation, with polyimides (PI), polybenzimidazole (PBI) and their derivatives leading the field [6,7]. Benzimidazole-linked polymer (BILP), featuring branched, fused-ring architectures analogous to PBI, has shown enhanced free-volume porosity and gas permeability alongside outstanding thermal and chemical resilience, marking them as promising candidates for high-temperature hydrogen purification applications [8–10]. Initially, BILP materials were primarily reported in powder form, posing significant challenges for membrane fabrication. Shan et al.

* Corresponding authors.
E-mail addresses: mxshan@zzu.edu.cn (M. Shan), dyli@zzu.edu.cn (D. Li).

Peer review under the responsibility of Editorial Board of Green Energy & Environment

https://doi.org/10.1016/j.gee.2025.12.020

pioneered the interfacial polymerization method to successfully prepare BILP-101 membranes for hydrogen separation [11,12]. Although a variety of BILP architectures have been reported, only BILP-5 and BILP-101 have been studied for H_2/CO_2 separation, leaving other members of this family largely unexplored [13]. Motivated by the exceptional H_2/CO_2 separation performance of BILP-101 membrane, the systematic screening and membrane fabrication of other BILP architectures, coupled with a thorough evaluation of their H_2/CO_2 separation properties, are critically needed. However, traditional experimental approaches for such extensive material screening are inherently time- and resource-intensive. In contrast, molecular simulation techniques offer a powerful avenue to directly probe the microscopic interactions and transport pathways governing gas permeation [14,15]. Furthermore, in silico screening of virtual BILP candidates can significantly accelerate the discovery of promising membrane designs, thereby guiding targeted synthesis and substantially reducing experimental burden [16].

Molecular simulation has become an essential tool for the design and optimization of gas separation membranes, with broad applications across covalent organic frameworks (COFs), polymers of intrinsic microporosity (PIMs), and related materials [17–19]. However, computational investigations of BILPs remain limited despite their promising separation performance. Liu et al. [20] employed classical simulation configuration, consisting of molecular dynamics (MD) and grand canonical Monte Carlo (GCMC), to evaluate CO_2/CH_4 separation in BILP-4, elucidating that CO_2-induced plasticization alters pore dimensions. Similarly, Duan et al. [13] applied the simulation strategy to BILP-5 for H_2/CO_2, demonstrating that diffusion governs selectivity, though simulated permeation rates are lower than experimental values, underscoring the need for improved force fields and modeling protocols. The three-dimensional porous architectures of BILPs, which play a pivotal role in governing gas transport, remain insufficiently characterized by existing simulation frameworks, thereby limiting mechanistic understanding of H_2 separation. To address this gap, a comprehensive molecular model and simulation study is urgently needed to construct reliable atomistic models and elucidate the mechanisms underlying H_2/CO_2 separation. In addition, the structural properties of BILP-101 vary significantly depending on synthesis method: BILP-101 powders synthesized in DMF show a specific surface area of 460 m^2/g [21], whereas BILP-101 films fabricated at the aqueous–organic interface exhibit only 87 m^2/g [11], likely due to differences in chain conformation. While experimental techniques face challenges in probing such microscopic variations, molecular simulations offer a powerful means to elucidate the three-dimensional architecture and H_2 separation performance of BILPs.

Building on our prior work with BILP-101, the molecular models with diverse BILP chain architectures were built to predictively evaluate selectivity. Key microstructural descriptors were computed and correlated with transport properties to elucidate the atomistic mechanisms underlying H_2/CO_2 separation. To validate the robustness and generality of our approach, we extended the simulations to H_2/N_2 and H_2/CH_4 mixtures across a range of temperatures, achieving excellent agreement with experimental data. Finally, a bridge between theoretical computation and experiment was established through the fabrication of a BILP-15 membrane via interfacial polymerization and the subsequent evaluation of its H_2/CO_2 separation performance, revealing strong consistency with our theoretical predictions. This study overcomes the constraints of conventional approaches—namely the reliance on single configurations and limited selectivity prediction—by developing a transferable BILP model capable of elucidating H_2 separation mechanisms across varied conditions.

2. Materials and methods

2.1. Fabrication of supported BILP-15 membranes

The α-Al_2O_3 supports were first immersed in dichloromethane solutions of 1,2,4,5-tetrakis (4-formylphenyl) benzene (TFPB, 97%) (0.77, 0.50, and 0.25 wt%) containing 1.0 mol/L acetic acid for 30 min. After removal, the supports were air-dried at ambient conditions until no visible solvent droplets remained on the surface. Each support was then transferred to aqueous solutions of 3,3-diaminobenzidine tetrahydrochloride (DAB, 99%) (1.5, 1.0 and 0.5 wt%) and allowed to react for 2 h. The membranes were removed, dried overnight at room temperature, and subsequently cured in an oven at 403 K ($\approx$130 °C) for 72 h, yielding the BILP-15 composite films. Finally, the membranes were washed sequentially with deionized water and dichloromethane (3 min each) to remove residual monomers, dried overnight in a fume hood, and then used for gas-permeation measurements.

2.2. Model construction

The BILP-101 framework was constructed using *Materials Studio* [22]. Adapting the molecular dynamics methodology pioneered by Duan et al. [13], we implemented an all-atom computational framework to simulate polymer–gas interactions. A comprehensive force field comparison was conducted, evaluating three widely used parameter sets: COMPASS [23,24], PCFF [25,26] and GAFF [27]. The GAFF force field parameters were adapted from the protocol established by Athri et al. [28], whereas COMPASS and PCFF retained their default parameterizations as implemented in *Materials Studio*. The charges for both the polymers and gases were set according to the default charges of the PCFF and COMPASS force fields, respectively. Based on the actual fabrication process, an aldehyde group is used to terminate the BILP-101 chain. For spatial polymers, conformational variations significantly impact structural fidelity and predictive accuracy. To systematically evaluate these effects, three representative configurations were selected (Fig. 1a). L-type: Linear, unbranched topology; Y-type: Symmetrical branching extending radially from a central node; X-type: Multidirectional branching network with complexity progressively increasing to approximate experimental configurations. The nomenclature L-*n*, Y-*n*, and X-*n* denotes the

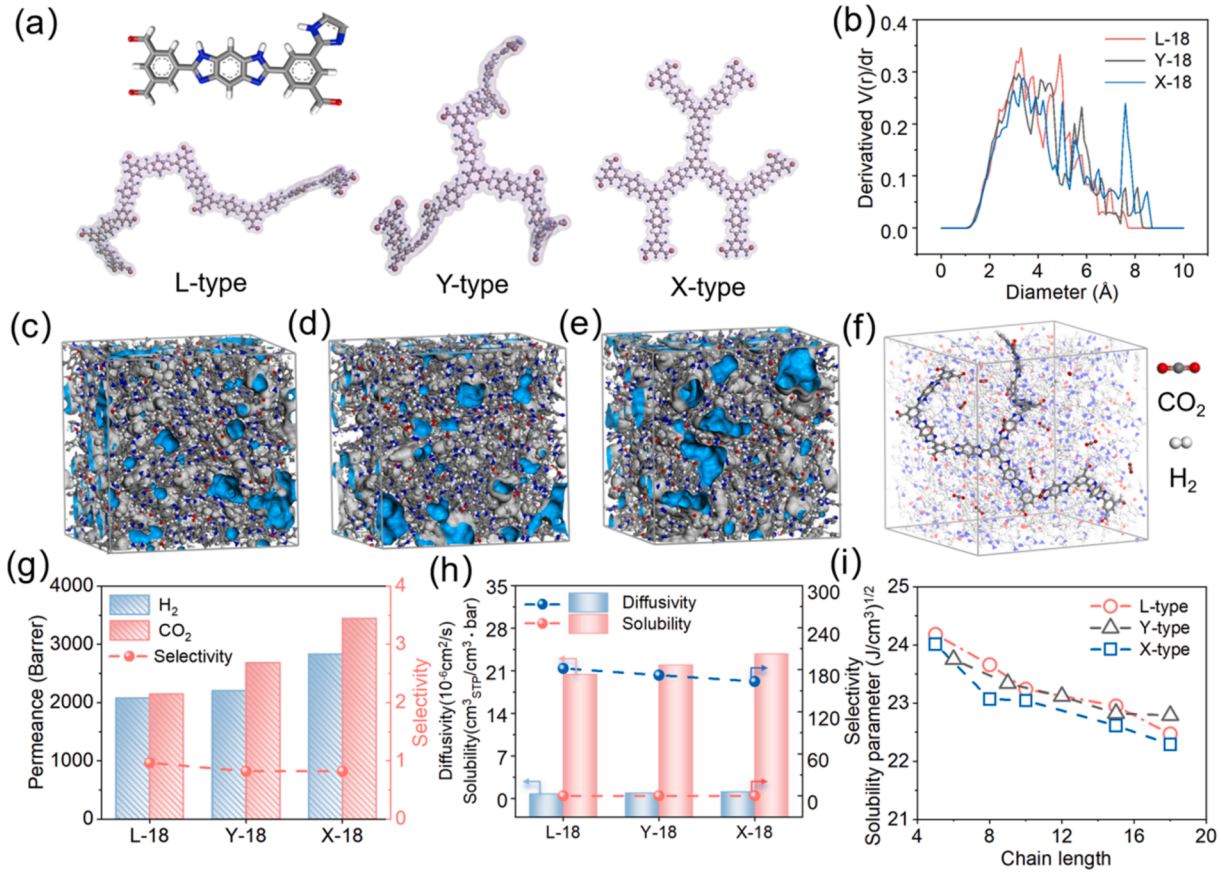

Fig. 1. The physicochemical properties and structural properties of different configurations. Structural formulas of different conformations: (a) L-type, Y-type, X-type. (b) The pore size distribution obtained by our method. The accessible space of probe molecule with radius of 1.455 Å, (c) L-18. (d) Y-18. (e) X-18. (f) Snapshot of equilibrated model with permeation of H_2/CO_2 gas mixtures. H_2/CO_2 separation performance of BILP-101 membranes under different chain conformation: (g) Permeance and selectivity at 298 K and 1 bar, (h) CO_2 adsorption and diffusivity, and corresponding H_2/CO_2 selectivity, (i) Solubility parameters with chain-length variation.

degree of polymerization, where *n* specifies the monomer count per chain (Table S1).

The conventional equilibrium method, previously validated for accurately predicting properties such as density and glass transition temperature (T_g), was adopted as the baseline. Our simulation protocol incorporates several modifications, described as follows.

Step 1: Construct the BILP-101 chain using the COMPASS force field and pack the chains into an amorphous cell with an initial density of 0.5 g/cm^3;
Step 2: Perform energy minimization to optimize the structural configuration;
Step 3: Conduct MD simulations at 600 K, gradually increasing the system density over 50 ps;
Step 4: Execute six heating−annealing cycles by cooling from 600 K to 300 K every 50 ps, increasing the pressure from 1 atm to 100 atm, and subsequently reducing it to 1 atm to achieve equilibrium;
Step 5: Apply the PCFF force field for a temperature-annealing cycle on the equilibrated structure. After stabilization, switch to the COMPASS force field and repeat the annealing process until the structural parameters converge;
Step 6: Assign PCFF-derived partial charges to the polymer, repeat the heating−annealing cycle, and terminate once the model exhibits structural stability.

MD simulations were conducted using the *Materials Studio* software package. Non-bonded interactions were truncated at a cutoff distance of 15.5 Å for both Van der Waals (vdW) and electrostatic terms. The simulations employed the velocity-Verlet integrator with a 1 fs timestep, and energy minimization was performed using the conjugate gradient algorithm until convergence criteria were met. Temperature and pressure regulation, where applicable, was achieved using Nosé-Hoover thermostat and barostat chains. The specific equilibrium steps are recorded in the Supplementary Materials.

Gas solubility coefficients were computed through GCMC [29,30] simulations, involving an equilibration period of 10^7 MC cycles followed by a production run of 10^7 MC cycles [31]. Since the chemical potential corresponds directly to

pressure, the Peng–Robinson equation [32] was used to compute the chemical potential of gases, thereby linking it to pressure. Further details on the GCMC settings can be found in the literature [33]. Simulations were conducted to calculate the adsorption isotherms of single-component gases at 300 K and within a pressure range of 0-10 bar. Diffusivity coefficients were derived from mean square displacements (MSDs) using MD simulations in the NVT ensemble, conducted over 2×10^3 ps. Given the excellent stability of BILP-101 at high temperatures, the conformations simulated in this study were equilibrated at 300 K and 1 bar.

Materials Studio was used to calculate the solubility parameter (δ) and radial distribution function (RDF), and to calculate the equilibrium model under NVT conditions for 200 ps. The Zeo++ program [34,35] was used to measure the pore size distribution (PSD), global cavity diameter (GCD), and specific surface area of polymers. The probe molecule radius of PSD and GCD is 0.5 Å, and the specific surface area measurement is consistent with the experiment, using a probe molecule radius of 1.82 Å.

3. Results and discussion

3.1. Investigation on chain conformation

Polymer conformation is a critical determinant of physicochemical properties [36,37], directly influencing the pore architecture and thus the separation performance of prepared membranes [36]. The experimentally observed variations in specific surface area of BILP-101 were contributed to the configuration-dependent pore architectures. To investigate this, three representative chain conformations, unbranched linear (L-type), centrally branched (Y-type), and multi-directionally branched (X-type) configurations were employed in our models (Fig. 1a). BILPs powders with higher porosity formed in DMF primarily adopt the larger-pored X-type structure, whereas BILPs membrane films with lower derived from interfacial polymerization likely possess fewer X-type chains. To elucidate the dominant chain architecture in these membranes and its implications for separation performance, the separation performance of each configuration was systematically evaluated.

Based on our previous modeling work [13], BILP-101 was constructed using both conventional and newly optimized methods, employing a representative chain length of 18. The resulting pore size distributions are shown in Fig. 1b and Fig. S1. Under the conventional approach (Fig. S1), an increased branching degree, from L-type to X-type, resulted in a greater proportion of large pores. While our optimized method exhibited similar trends, the distributions were notably smoother and contained fewer excessively large pores (Fig. 1b), indicating a significant improvement in structural realism. Fractional free volume (FFV) snapshots for L-, Y-, and X-type configurations (Fig. 1c–e) further corroborate these observations. Consistent with the pore size analysis, calculated FFV values followed the order of X-18 > Y-18 > L-18, suggesting a potential overestimation of porosity in the X-18 model. Similar trends were observed for overall porosity and GCD. Notably, our refined method not only reproduced the correct order of porosity but also yielded lower absolute values, reflecting a more compact and realistic polymer structure (Table S2 and S3).

Fig. 1f shows a representative snapshot of the equilibrated BILP-101 model constructed with a typical chain architecture of Y-type, illustrating H_2 and CO_2 molecules adsorption and diffusion within the matrix. To investigate the impact of polymer architecture on gas separation performance, BILP-101 models with varying degrees of chain branching were evaluated using our optimized modeling approach (Fig. 1g and h). As shown in Fig. 1g, both H_2 and CO_2 permeabilities increased with increasing branching degree. However, the H_2/CO_2 selectivity exhibited an inverse trend, decreasing in the order L-type > Y-type ≥ X-type. This inverse relationship is directly linked to the emergence of larger pores with increasing branching density, as evidenced by steeper MSD curves (Fig. S2a and b) and an increased prevalence of 8-10 Å pores (Fig. 1b, Table S2). These larger pores introduce additional free volume and adsorption sites that preferentially accommodate larger CO_2 molecules, thereby diminishing molecular sieving capability. The increase in both D_i and S_i (Fig. 1h) further supports the view that transport is increasingly dominated by physical diffusion mechanisms in branched configurations. Importantly, binding energy calculations (Table S4, Fig. S2d) reveal negligible variation across configurations, conclusively demonstrating that structural characteristics, rather than gas-polymer interaction strength, govern the separation performance. This finding is further corroborated by RDF analyses, which show stronger interchain interactions in the L-type model compared to Y- and X-type variants (Fig. S2c and d), contributing to its more constrained pore environment. Collectively, these results underscore that excessive branching compromises membrane selectivity by promoting larger pore formation and undermining size-sieving efficiency. While fully linear chains maximize selectivity, they may deviate from realistic polymer network structures. In contrast, the Y-type configuration emerges as an optimal compromise, uniquely balancing manageable branching with a well-balanced pore structure.

The δ is widely used as a benchmark for evaluating the physical relevance and reliability of polymer models. To further assess the validity of our modeled configurations, we computed and compared the δ values for L-type, Y-type, and X-type architectures across varying chain lengths. As shown in Fig. 1i, both L-type and X-type models exhibited significant fluctuations in δ with chain length, indicative of structural instability or incomplete convergence within the simulated networks. In contrast, the Y-type configuration displayed a consistent decrease in δ that levelled off with increasing chain length, in strong agreement with established polymeric behavior, for which δ decreases with increasing chain length before reaching a plateau [38,39]. These results strongly support the Y-type configuration as the most physically reasonable among the three, reinforcing its suitability for constructing realistic polymer network models of BILP-101.

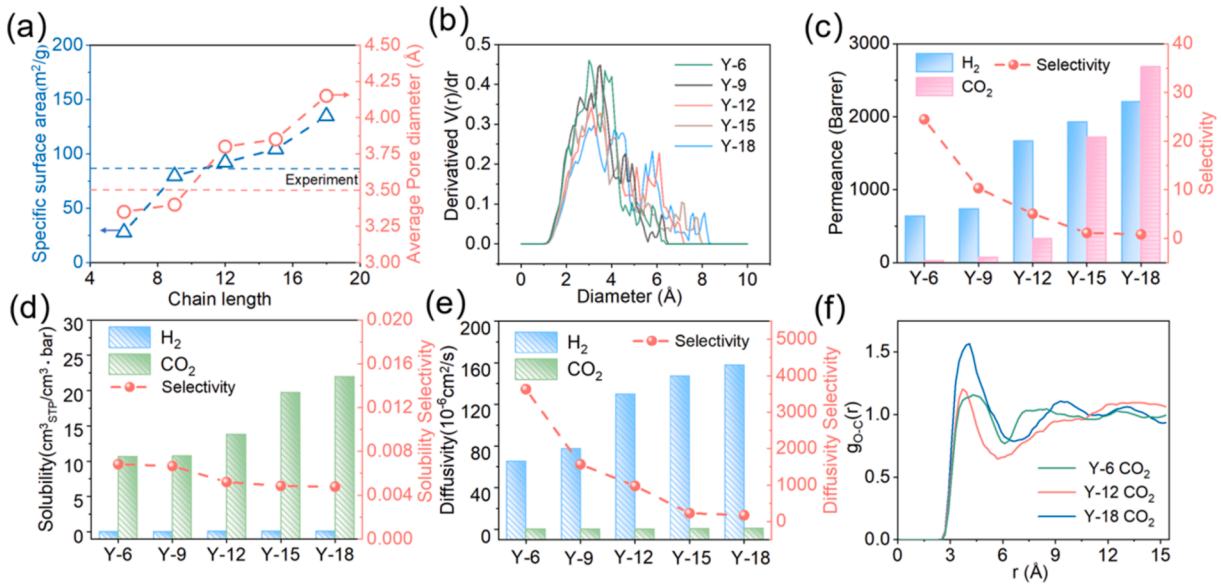

Fig. 2. Comparison of different chain lengths in Y-type configurations. (a) Specific surface area and average pore size [11]. (b) Pore size distribution. (c) H_2/CO_2 selectivity and permeance at 298 K and 1 bar. (d) Adsorption selectivity. (e) Diffusion selectivity; (f) $g_{C\text{-}O}(r)$ between BILP-101 and CO_2.

Comprehensive evaluation of structural features, separation performance, and solubility parameters identifies the Y-type architecture as the most suitable configuration among the three candidates. Its balanced topology supports both structural integrity and favorable gas transport characteristics, suggesting that Y-type structures likely dominate the polymer network in BILP membranes synthesized via interfacial polymerization, while L-type and X-type configurations contribute in secondary roles. However, despite the Y-type's optimized architecture, all configurations exhibit limited H_2/CO_2 selectivity, indicating that polymer topology alone does not fully account for the experimentally observed separation behavior. This suggests that factors beyond branching morphology are critical determinants of separation performance. To address this, we extended our investigation to examine the influence of polymer chain length, using the Y-type configuration as a structural baseline. This approach isolates the impact of chain length as a distinct variable and provides further insight into the structure–property relationships governing membrane performance.

3.2. Chain length dependence

Using the Y-type configuration, we proceeded to assess how specific surface area and average pore size reflect structural characteristics, enabling direct comparison with experimental data [19]. Computational simulations demonstrated that increasing chain length beyond 12 units resulted in a notable enhancement in surface area and average pore size, associated with the formation of larger pores (Fig. 2a, Fig. S3). Further structural analysis across varying chain lengths consistently demonstrated decreasing model density and increasing FFV, GCD, and PSD values (Fig. 2b, Fig. S4 and Table S3 and S5), thereby suggesting that longer chains reduce packing efficiency. Considering both structural trends and alignment with experimental surface area of 87 m^2/g [11], a chain length of approximately 10 units appears to provide a reasonable balance.

The gas separation performance of Y-type BILP-101 was evaluated across varying chain lengths. As chain length increased, both H_2 and CO_2 permeabilities rose, while H_2/CO_2 selectivity gradually declined (Fig. 2c). This trend is attributed to simultaneous increases in gas diffusivity and solubility (Fig. 2d and e), driven by enhanced porosity and larger GCD in longer-chain models. Adsorption selectivity similarly decreased with chain elongation before reaching a plateau, consistent with the expansion of pore networks and the emergence of additional adsorption sites. This is further supported by the stronger first-peak intensities in radial distribution functions for longer chains, particularly Y-18 (Fig. 2f), and corroborated by adsorption isotherms (Fig. S5). Given the smaller kinetic diameter of H_2, shorter-chain models exhibit higher adsorption selectivity, which stabilizes as additional, less selective pores are introduced at longer lengths. These results highlight a critical permeance-selectivity trade-off inherent to polymer chain length in BILP membranes.

Diffusion selectivity across Y-type BILP-101 models with varying chain lengths was further analyzed (Fig. 2e, Fig. S6). Shorter chains exhibited reduced diffusivity for both H_2 and CO_2, but significantly enhanced H_2/CO_2 diffusion selectivity. This sharp increase is attributed to the formation of smaller pores (2.9–3.3 Å) as chain length decreases (Fig. 2b), which preferentially restrict CO_2 transport while allowing H_2 to diffuse. In contrast, longer chains generate larger pores that diminish molecular sieving effects, thereby reducing selectivity. Overall, the decline in H_2/CO_2 selectivity with increasing chain length is primarily governed by changes in diffusivity, with solubility plays a comparatively minor role.

Table 1
Comparison of BILP-101 performance modeled by different methods [9]. The letter *i* stands for hydrogen and *j* stands for carbon dioxide.

Method	Conventional		This work	
Density (g/cm^3)	1.252		1.271	
	H_2	CO_2	H_2	CO_2
S(cm$^3_{STP}$/(cm^3·bar))	1.02×10^{-1}	40.09	7.17×10^{-2}	10.76
$\alpha_{S(i/j)}$	2.54×10^{-3}		6.66×10^{-3}	
D(cm^2/s)	2.62×10^{-4}	5.45×10^{-7}	7.75×10^{-5}	5.00×10^{-8}
$\alpha_{D(i/j)}$	480.73		1550.00	
P(Barrer)	3571.94	2912.95	740.25	71.74
$\alpha_{sim(i/j)}$	1.23		10.32	
$\alpha_{exp(i/j)}$	10.13			

Binding energy profiles across chain lengths consistently support this conclusion (Fig. S7), aligning with previous studies [9,20]. Similar trends were observed for L-type and X-type configurations (Fig. S8–S13), indicating the robustness of this behavior across topologies. Chains that are too short are experimentally impractical, while excessively long chains impair separation performance. Balancing structural fidelity with functional efficiency, a chain length of approximately 10 units is optimal. Therefore, the Y-type configuration with 10-unit chains—represented here by the Y-9 model—was selected for subsequent analyses.

3.3. Discussion of simulation protocol

3.3.1. Separation performance

The gas separation performance predictions for the BILP-101 membrane were compared using the conventional and our optimized simulation protocols (based on the Y-9 model), as summarized in Table 1. The density calculated using our new protocol (1.274 g/cm^3) is slightly higher than that from the conventional one (1.252 g/cm^3). While both values remain below the experimental measurement (1.65 g/cm^3). This discrepancy is anticipated, as experimental density is typically measured via gas displacement, which neglects internal porosity and can lead to overestimation. Both methods overpredict gas permeance relative to experimental values, consistent with prior reports on the limitations of the GCMC + MD approach [16,40,41]. As noted by Jiang et al. [20], this simulation framework evaluates permeance through the solution-diffusion model, which often overestimates diffusion coefficients and, consequently, permeance. Crucially, despite these general limitations, our optimized method yields significantly more accurate selectivity predictions. The calculated separation factor ($\alpha_{sim(i/j)} = 10.32$) closely matches the experimental value ($\alpha_{exp(i/j)} = 10.13$) [9], whereas the conventional one produces a much lower value ($\alpha_{sim(i/j)} = 1.23$). These results demonstrate that our modeling framework offers a substantially improved prediction of BILP-101 membrane performance, particularly for selectivity, which is a critical parameter in gas separation applications.

The accuracy of this protocol was further validated using additional gas pairs (H_2/CO_2, H_2/N_2, H_2/CH_4). The simulated selectivities ($\alpha^{sim}_{H_2/CO_2} = 20.65$, $\alpha^{sim}_{H_2/N_2} = 43.53$, and $\alpha^{sim}_{H_2/CH_4} = 35.60$) closely match the experimental values ($\alpha^{exp}_{H_2/CO_2} = 20.95$, $\alpha^{exp}_{H_2/N_2} = 41.21$, and $\alpha^{exp}_{H_2/CH_4} = 31.16$), demonstrating strong agreement across different gas mixtures (Fig. 3a and Fig. S14–S16). Furthermore, the temperature-dependent H_2/CO_2 separation performance also showed excellent consistency between simulations and experiments (Fig. 3b and Fig. S14). These results confirm that our modeling framework reliably predicts gas separation selectivity across diverse gas mixtures and operating conditions.

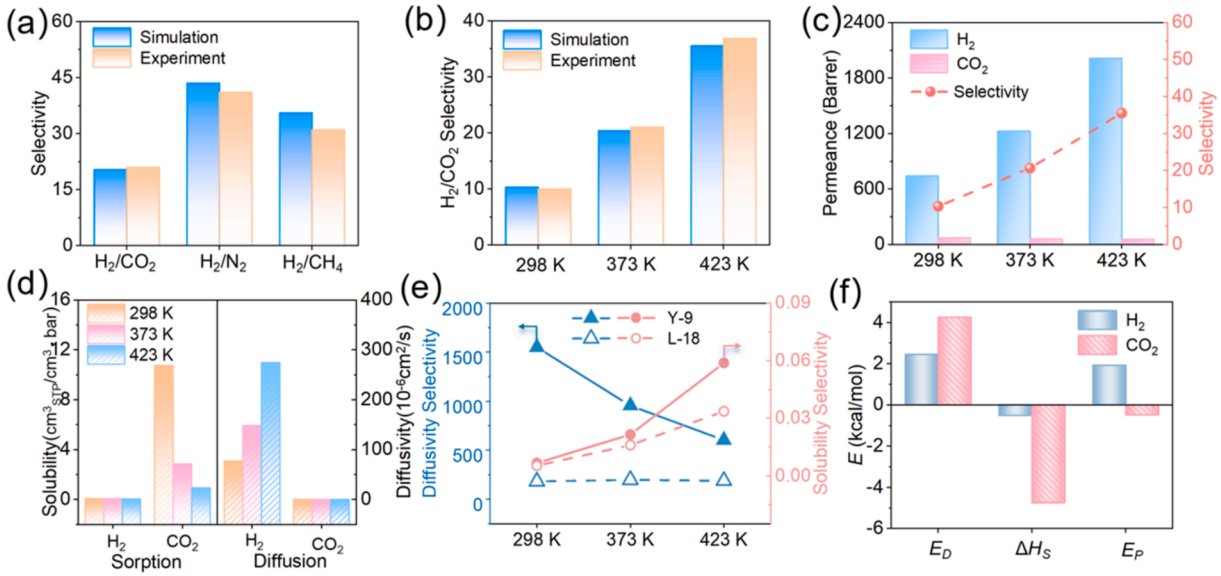

Fig. 3. Comparison of different chain lengths in Y-type configurations. (a) Selectivity for different gases at 373 K and 1 bar. (b) H_2/CO_2 selectivity at different temperatures and 1 bar [9]. Separation performance at different temperatures, (c) H_2 and CO_2 separation performance. (d) H_2 and CO_2 adsorption and diffusion at 1 bar. (e) Adsorption and diffusion selectivity. (f) Activation energy for diffusion (E_D), sorption enthalpy (ΔH_S), and activation energy for permeation (E_P) of H_2 and CO_2.

3.3.2. Temperature dependence

Although extensive research has examined membrane stability at high temperatures, the underlying separation mechanisms across varying temperatures remain poorly understood and thus are systematically investigated in this study. Using the Y-9 model, our simulations (Fig. 3c) reveal that H_2 permeance increases with temperature, while CO_2 permeance decreases, resulting in enhanced H_2/CO_2 selectivity. This trend is driven by counteracting temperature responses in adsorption and diffusion: diffusion coefficients rise, while adsorption capacities decline for both gases (Fig. 3d). Further analysis using the Y-9 model clarifies the underlying mechanisms. As shown in Fig. 3e, H_2/CO_2 adsorption selectivity increases with temperature due to the pronounced desorption of CO_2, while H_2 uptake remains largely unaffected because of its weak interaction with the framework. Consequently, CO_2 adsorption decreases significantly, whereas H_2 shows only a minor decline, leading to improved selectivity at elevated temperatures. In contrast, diffusion selectivity decreases with rising temperature. At room temperature, restricted chain mobility and narrow pore size distribution hinder CO_2 diffusion. With increasing temperature, enhanced polymer chain flexibility and pore expansion facilitate CO_2 transport, as shown in Fig. S17 and S18. H_2 diffusion remains relatively stable due to its smaller kinetic diameter and lower sensitivity to temperature (Figs. S17–S18).

Following Oh et al. [42], the E_D and H_S contributions were calculated using Eqs. S6 and S7, respectively. A positive E_D denotes energetic-driven selectivity (enhanced diffusivity with rising temperature), whereas a negative H_S indicates enthalpy-driven selectivity (reduced adsorption at higher temperatures) (Fig. 3f, Fig. S15b). The relative magnitudes of E_D and H_S determine temperature-dependent separation behavior, with larger disparities intensifying their effects. For BILP-101, ΔH_S is 2.32 times greater than ΔE_D, indicating adsorption-dominated temperature sensitivity. To further identify the dominant mechanism, the energetic parameter was evaluated: positive E_P values correspond to diffusion-controlled behavior, while negative values indicate adsorption-controlled selectivity. The calculated E_P for CO_2 (−2.03 kJ/mol) confirms enthalpy-driven selectivity in BILP-101, consistent with its adsorption-controlled temperature response (Fig. 3e).

While this aligns with the experimental trend, a slight discrepancy in CO_2 permeance may arise from its inherently low value and methodological differences between simulation and experiment. Overall, these results confirm that both diffusion and adsorption controlled the gas separation processes in BILP-101, with adsorption demonstrating a somewhat stronger influence across the examined temperature range.

3.3.3. Charges effects

Gas solubility in polymer membranes is primarily governed by intermolecular interactions, including Lennard-Jones (LJ) potentials and electrostatics. LJ interactions depend on the potential form and associated force field parameters, while electrostatic interactions are dictated by atomic charge assignments. Unlike conventional approaches, our simulation protocol actively regulates both non-bonded parameters and atomic charges during the simulation process. To account for variability in force field behavior, three representative force fields (COMPASS, PCFF, and GAFF) were employed for comparative analysis. Charge values were determined using both density functional theory (DFT) calculations and standard force field defaults [43–45]. To evaluate the role of electrostatics in gas separation, multiple force field-charge set combinations were systematically investigated, revealing the sensitivity of performance predictions to these parameters.

Effect of Gas Charges. For elemental gases like H_2, the charge is fixed at zero. In contrast, CO_2 charge values vary depending on the chosen force field. The impact of different LJ and charge parameter combinations on membrane performance was evaluated (Table 2, Fig. 4a and b), where C(q) and P(q) represent CO_2 charges derived from the COMPASS and PCFF force fields, respectively. As shown in Table 2, using native COMPASS or PCFF parameters yields poor H_2/CO_2 selectivity (4.88 and 0.65, respectively). However, substituting PCFF-derived charges (P(q)) into the COMPASS framework significantly improves selectivity to 14.65 (Fig. 4a). This enhancement stems from reductions in CO_2 solubility and diffusivity, while H_2 properties remain largely unchanged (Fig. 4b, Fig. S19 and S20). Specifically, within the COMPASS force field, switching the gas charge model from C(q) to P(q) reduces the CO_2 adsorption capacity from 22.94 to 11.59 $cm^3_{STP}/(cm^3 \cdot bar)$. The resulting increase in both adsorption and diffusion selectivity accounts for the overall improvement in separation performance. CO_2 adsorption isotherms under identical LJ parameters but varying charge sets (Fig. S21) further validate this finding. Conversely, replacing P(q) with C (q) under the PCFF force field increases CO_2 solubility and diffusivity, confirming the critical role of electrostatics in tuning separation behavior.

Effects of Polymer Charge. The influence of BILP-101's atomic charges on membrane performance was also assessed (Table 2, Fig. 4d and e), using a fixed CO_2 charge set (P(q)) within both COMPASS and PCFF frameworks. As shown in Fig. 4e and Fig. S21b, modifying the polymer charges had minimal impact on CO_2 adsorption (e.g., a negligible change from 11.59 to 10.76 $cm^3_{STP}/(cm^3 \cdot bar)$ under COMPASS),

Table 2
Comparison of H_2/CO_2 separation performance upon charge and force field transformation. Where LJ and q represent force field and charge, respectively, and C and P represent COMPASS and PCFF, respectively.

	Polymer		Gas (CO_2)		Membrane Performance		
	LJ	q	LJ	q	P (Barrer)		$\alpha_{P(i/j)}$
					H_2	CO_2	
Model obtained by	C	C	C	C	1018.36	208.55	4.88
COMPASS force fields	C	C	C	P	1018.36	69.53	14.65
equilibrium	C	P	C	P	740.25	71.74	10.32
Model obtained by PCFF	P	P	P	P	71.44	109.90	0.65
force fields equilibrium	P	P	P	C	71.44	230.45	0.31
	P	C	P	P	136.59	102.73	1.32

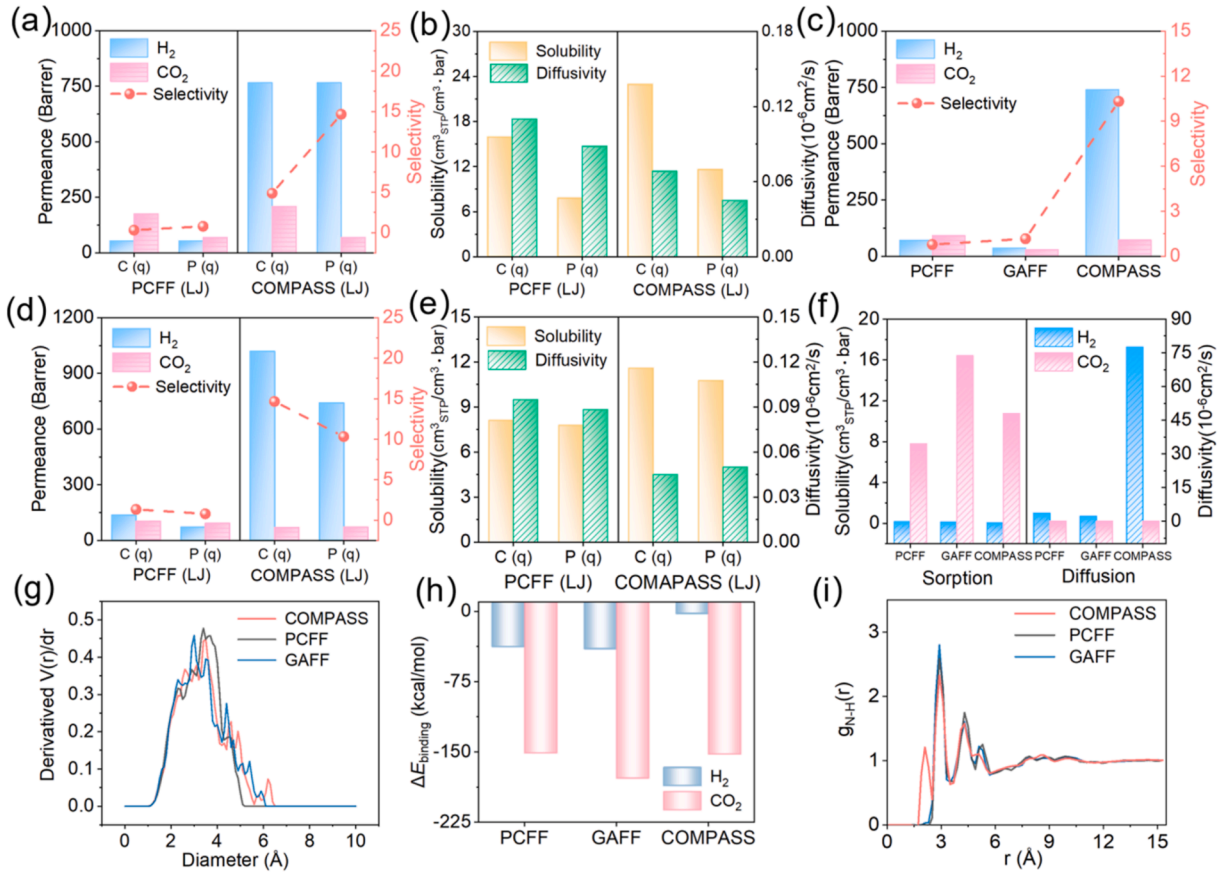

Fig. 4. Comparison of different charges and force fields in the Y-9 model. Changes in gas charges (a, b) and polymer charges (d, e). (a, c, d) H_2/CO_2 selectivity and permeance at 298 K and 1 bar. (b, e) CO_2 adsorption and diffusion. C(q) and P(q) represent the COMPASS and PCFF charges, respectively, while COMPASS (LJ) and PCFF (LJ) denote the COMPASS and PCFF force fields, respectively. (f) H_2 and CO_2 adsorption and diffusion at 298 K and 1 bar. (g) Pore size distribution. (h) Gas-polymer binding energy; (i) $g_{N\text{-}H}(r)$ between N and H atoms of BILP-101.

indicating that adsorption is primarily governed by gas charges rather than polymer charges. In contrast, notable differences in gas permeance, solubility, and diffusivity were observed across force fields, irrespective of whether changes were applied to the gas or polymer components. These results highlight the dominant role of LJ potential parameters in controlling gas transport behavior and emphasize their importance in ensuring the predictive reliability of the simulation model.

3.3.4. Force field effects

Force field selection is known to significantly influence molecular simulation outcomes [46–48], as exemplified by the substantial variations in ZIF adsorption selectivity observed with different parameterizations [47]. Building on this, the gas separation performance using three commonly adopted polymer force fields, including GAFF, COMPASS, and PCFF was systematically compared. A consistent charge set (P(q)) was applied to both CO_2 and BILP-101 to isolate the impact of LJ parameters. As shown in Fig. 4c, gas permeance and selectivity vary significantly across force fields. While GAFF and PCFF produced negligible selectivity, the COMPASS force field yielded results in close agreement with experimental data, highlighting its superior predictive accuracy in this system.

Analysis of adsorption and diffusion behavior (Fig. 4f) shows that CO_2 solubility decreases in the order GAFF > COMPASS > PCFF, a trend further supported by adsorption isotherms across force fields (Fig. S22). To quantify these interactions, binding energies ($\Delta E_{binding}$) between CO_2/H_2 and BILP-101 were calculated for each force field (Fig. 4h). The $\Delta E_{binding}$ values for CO_2 correlate well with its solubility, whereas H_2 shows minimal variation in solubility across force fields (PCFF ≈ GAFF > COMPASS), consistent with negligible changes in $\Delta E_{binding}$. However, the slightly stronger H_2-polymer interactions predicted by PCFF and GAFF likely hinder H_2 diffusion, suppressing its permeance and resulting in lower CO_2/H_2 selectivity (Fig. 4e and f).

To isolate the effect of structural factors, key parameters including density, porosity, FFV, and PSD were compared across models (Fig. 4g, Table S6 and Fig. S23). Structural metrics remained consistent across force fields, demonstrating that differences in H_2 permeance stem primarily from gas-polymer intermolecular interactions rather than microstructural variations. RDFs (Fig. 4i) reveal markedly stronger N···H interactions for PCFF than for COMPASS. This finding is mirrored in the pore-size distributions (Fig. 4g), for which PCFF exhibits enhanced inter-chain contacts and a correspondingly denser pore architecture. The observed force-field-

dependent coupling between local interaction strength and mesoscopic structure attests to the internal consistency and physical plausibility of our simulation protocol.

Accordingly, the model performance is strongly governed by both LJ and charge parameters. Adsorption behavior is primarily dictated by gas molecule charges, with minimal influence from polymer charges. In contrast, diffusion and overall separation performance are highly sensitive to force field selection. PCFF and GAFF significantly underpredict H_2 diffusion, resulting in poor selectivity. Only the COMPASS force field, combined with P(q), accurately reproduces experimental gas separation behavior, highlighting its superior predictive reliability.

3.4. Model transferability

To validate the transferability of the simulation approach, BILP-15 and BILP-5 were experimentally synthesized and modeled. Using the established simulation framework for BILP-101, single-chain models were constructed with Y-12 and Y-9 configurations for BILP-15 and BILP-5, respectively. Both systems reached stable equilibration under the simulation protocol, with final structures and performance metrics summarized in Fig. S24.

Building on previous work with BILP-5 [13], BILP-15 was synthesized via interfacial polymerization (Fig. 5a). Experimental data for BILP-5 were obtained from previous experiments, whereas those for BILP-15 were generated through experimental work conducted in this study. Successful synthesis of BILP-15 was confirmed by ^{13}C CP/MAS NMR (Fig. 5b), with the characteristic N═C peak at 151 ppm indicating benzimidazole ring formation from DAB and TFPB monomers. Additional peaks at 112, 118, 130, and 142 ppm further confirm incorporation of the monomers into the polymer network. Cross-sectional and surface scanning electron microscopy (SEM) and atomic force microscopy (AFM) images (Fig. 5c and d) show that the BILP-15 film, prepared at 1.5 wt% DAB, is smooth, dense, and defect-free, though slight bubble morphology is observed due to solvent evaporation. Membrane thickness increases with monomer concentration (Fig. S25), consistent with enhanced polymer growth during interfacial polymerization. Additional characterization data are provided in Fig. S25–S27 and Table S7–S8. Subsequently, we conducted experimental testing and simulation verification on the supported BILP-15 membrane.

Using multiple simulation methodologies, the PSDs of BILP-5 and BILP-15 (Fig. S28)were computed, further

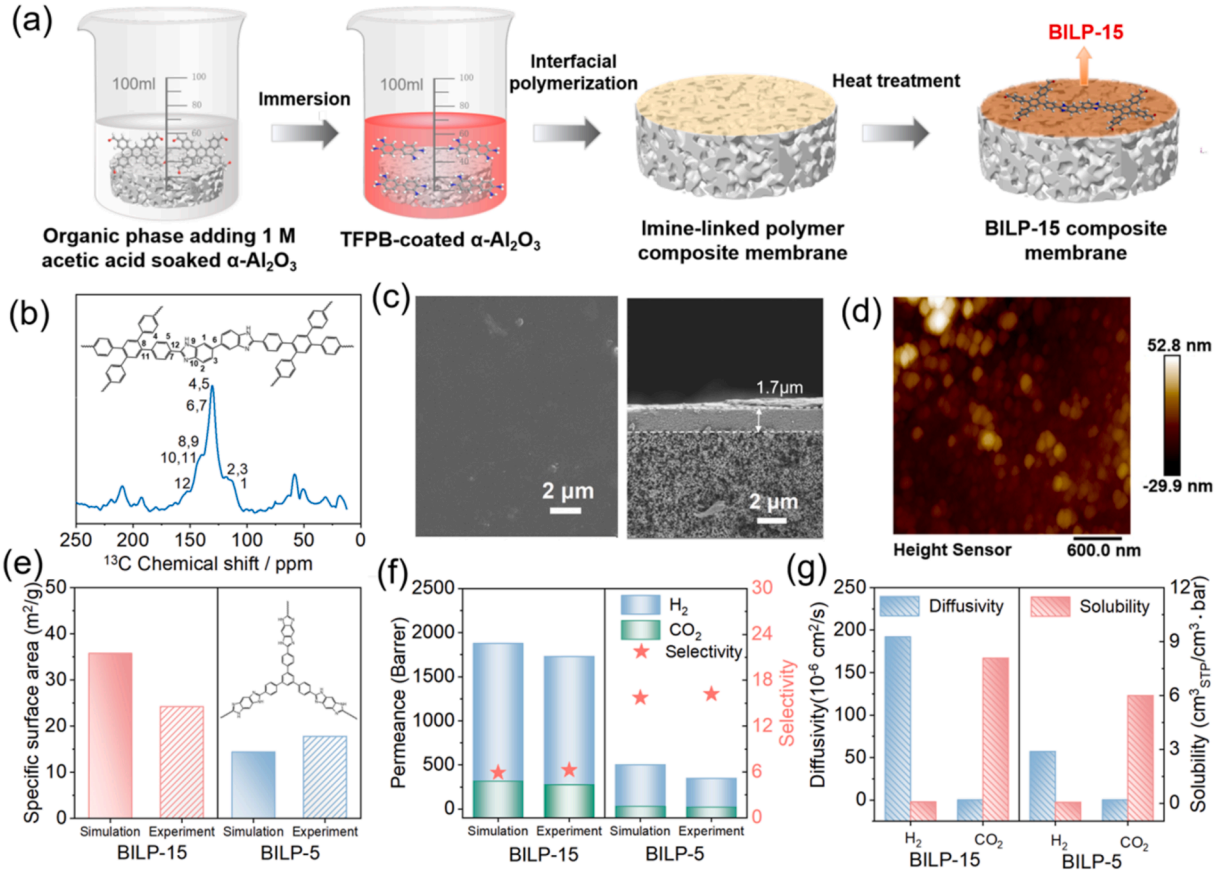

Fig. 5. Comparison of simulated and experimental values of BILP-15 and BILP-5 [13]. (a) Scheme of the synthesis of the α-Al_2O_3 supported BILP-15 membrane. (b) ^{13}C CP/MAS spectrum. (c) Cross-sectional and surface scanning electron microscopy (SEM) images of a BILP-15 membrane formed on alumina substrate. (d) Atomic force microscopy (AFM) topographical image of the film. (e) Specific surface area. (f) H_2/CO_2 selectivity and permeance at 298 K and 1 bar. (g) CO_2 adsorption and diffusion.

confirming robustness of our approach in accurately capturing BILP microstructures. Notably, the reduced frequency of large pores mirrors trends observed in BILP-101. Simulated surface areas closely match experimental values (Fig. 5e), with minor discrepancies attributable to well-known methodological differences in microporous material characterization [20]. The simulated H_2/CO_2 permeance and selectivity show strong agreement with experimental data (Fig. 5f). The simulated selectivity of BILP-15 is 5.91, demonstrating excellent agreement with the experimental value of 6.24. Similarly, for BILP-5, the simulated selectivity (15.71) corresponds closely to the experimental result (16.20). Overall, the deviation in selectivity is merely 3–5%, while permeability is slightly overestimated yet remains within the same order of magnitude. Diffusion and adsorption analyses (Fig. 5g) further reveal that diffusion selectivity closely tracks permeation trends, reinforcing the accuracy of the model [13]. These findings validate our force field-regulated simulation framework, which effectively suppresses large-pore artifacts and reliably predicts gas separation performance.

4. Conclusions

This study establishes a robust molecular modeling framework for accurately predicting the gas separation performance of BILP-101. The force field cycling protocol effectively refines pore structures, yielding strong agreement with experimental data. Comparative analysis of structural and separation metrics identified the Y-type configuration with a chain length of ~10 as the optimal model. Furthermore, our findings show that BILP-101's separation performance is primarily governed by diffusion selectivity, while temperature-dependent variations are rooted in the adsorption selectivity. Our results also show that gas molecule charge, not polymer charge, is the dominant factor in adsorption behavior. Under identical charge conditions, both PCFF and GAFF significantly underestimate H_2 diffusivity, reinforcing the superiority of COMPASS for accurate permeance predictions.

To validate the transferability of our modeling method, we extended the simulations to BILP-15 and BILP-5. The consistent results across all three systems confirm that the force field cycling method is a robust and transferable tool for establishing structure–property relationships in BILPs. This framework enables rational monomer screening and design for high-performance hydrogen separation membranes. The framework established for BILPs provides a robust methodological foundation that will be systematically extended to other polymer systems in future studies. Although molecular simulations offer invaluable atomistic insights, their high computational cost limits applicability in high-throughput screening. To address this limitation, a data-driven strategy leveraging machine learning (ML) is envisioned, given its proven capability in accelerating materials discovery [49–51]. Building on the work of Qiu et al. [51], future efforts will employ key physical descriptors (e.g., pore limiting diameter, density, porosity) and chemical features (e.g., elemental ratios, functional groups) as inputs to train ML models for predicting membrane permeability and selectivity. This integrated approach is expected to enable efficient screening of high-performance H_2 separation materials and expedite the development of next-generation membrane-based separation technologies.

CRediT authorship contribution statement

Qianqian Zhu: Writing − original draft, Visualization, Investigation. **Shaofan Duan:** Visualization, Investigation. **Meixia Shan:** Writing − review & editing, Supervision, Methodology, Conceptualization. **Freek Kapteijn:** Writing − review & editing. **Xin Gao:** Writing − review & editing, Validation. **Yatao Zhang:** Supervision, Project administration. **Dongyang Li:** Writing − review & editing, Validation, Supervision, Methodology, Investigation.

Data and materials availability

All data are available in the main text or the supplementary materials.

Declaration of competing interest

The authors declare that they have no known competing financial interests or personal relationships that could have appeared to influence the work reported in this paper.

Acknowledgments

This work was supported by the National Natural Science Foundation of China (No.22208317, 52473223, U2267225, U25A20608), China Postdoctoral Science Foundation (No. 2023M743172), Science and Technology Innovation Leading Talent Support Program of Henan Province (254000510023). The authors gratefully thank national Supercomputing Center in Zhengzhou (Zhengzhou University) for help and Dr. Zilong Liu from China University of Petroleum (Beijing) for providing the software and kind help with the simulation.

Appendix A. Supplementary data

Supplementary data to this article can be found online at https://doi.org/10.1016/j.gee.2025.12.020.

References

[1] T. Yurata, H. Lei, L. Tang, M. Lu, J. Patel, S. Lim, P. Piumsomboon, B. Chalermsinsuwan, C. Li, Int. J. Hydrogen Energy 44 (2019) 23120–23134.
[2] J.K. Nørskov, C.H. Christensen, Science 312 (2006) 1322–1323.
[3] B. Li, Z. Wang, Z. Gao, X. Han, Y. Li, Y. Ren, H. Huang, Adv. Funct. Mater. 33 (2023) 2300219.
[4] M. Carta, R. Malpass-Evans, M. Croad, Y. Rogan, J.C. Jansen, P. Bernardo, F. Bazzarelli, N.B. McKeown, Science 339 (2013) 303–307.
[5] W.S. Sun, M.J. Yin, W.H. Zhang, S. Li, N. Wang, Q.F. An, Green Energy Environ. 8 (2023) 1389–1397.

[6] H.B. Park, J. Kamcev, L.M. Robeson, M. Elimelech, B.D. Freeman, Science 356 (2017) eaab0530.
[7] J. Zhang, C. Niu, N. Ren, J. Du, M. Shan, R. Castro-Muñoz, Y. Zhang, Macromolecules 58 (2025) 3267–3277.
[8] M.G. Rabbani, H.M. El-Kaderi, Chem. Mater. 24 (2012) 1511–1517.
[9] M. Shan, J. Zhang, S. Cong, Y. Zhang, X. He, F. Kapteijn, X. Liu, Sep. Purif. Technol. 349 (2024) 127732.
[10] S. Cong, J. Wang, Z. Wang, X. Liu, Green Chem. Eng. 2 (2021) 44–56.
[11] M. Shan, X. Liu, X. Wang, I. Yarulina, B. Seoane, F. Kapteijn, J. Gascon, Sci. Adv. 4 (2018) eaau1698.
[12] A. Gao, X. Yan, S. Cong, X. Wang, H. Liu, Z. Wang, X. Liu, J. Membr. Sci. 668 (2023) 121293.
[13] S. Duan, D. Li, X. Yang, C. Niu, S. Sun, X. He, M. Shan, Y. Zhang, J. Membr. Sci. 671 (2023) 121396.
[14] J. Han, Z. Dong, L. Hao, J. Gong, Q. Zhao, Green Energy Environ. 8 (2023) 151–162.
[15] M. Chen, J. Zhou, J. Ma, W. Zheng, G. Dong, X. Li, Z. Tian, Y. Zhang, J. Wang, Y. Wang, Green Energy Environ. 10 (2025) 203–213.
[16] Q. Yang, D. Liu, C. Zhong, J.R. Li, Chem. Rev. 113 (2013) 8261–8323.
[17] G. Fan, D. Li, J. Wang, M. Shan, G. Dong, X. Feng, Y. Zhang, J. Membr. Sci. 716 (2025) 123503.
[18] G.S. Larsen, P. Lin, K.E. Hart, C.M. Colina, C.M. Lastoskie, Macromolecules 44 (2011) 6944–6951.
[19] Y. Ying, Z. Zhang, S.B. Peh, A. Karmakar, Y. Cheng, J. Zhang, C. Boothroyd, Y.M. Lam, Angew. Chem. Int. Ed. 60 (2021) 11318–11325.
[20] J. Liu, J. Jiang, J. Phys. Chem. C 123 (2019) 6607–6615.
[21] M. Shan, B. Seoane, A. Pustovarenko, A. Dikhtiarenko, J. Gascon, F. Kapteijn, J. Membr. Sci. 566 (2018) 213–222.
[22] M. Meunier, S. Robertson, Mol. Simul. 47 (2021) 537–539.
[23] H. Sun, P. Ren, J.R. Fried, Comput. Theor, Polym. Sci. 8 (1998) 229–246.
[24] M.J. McQuaid, H. Sun, D. Rigby, J. Comput. Chem. 25 (2004) 61–71.
[25] M.J. Hwang, T.P. Stockfisch, A.T. Hagler, J. Am. Chem. Soc. 116 (1994) 2515–2525.
[26] J.R. Maple, M.J. Hwang, T.P. Stockfisch, U. Dinur, M. Waldman, C. S. Ewig, A.T. Hagler, J. Comput. Chem. 15 (1994) 162–182.
[27] J. Wang, R.M. Wolf, J.W. Caldwell, P.A. Kollman, D.A. Case, J. Comput. Chem. 25 (2004) 1157–1174.
[28] P. Athri, W.D. Wilson, J. Am. Chem. Soc. 131 (2009) 7618–7625.
[29] Y. Wang, J. Wu, Y. Gao, K. Li, C. Wang, X. Cui, Green Energy Environ. 9 (2024) 1193–1198.
[30] Y. Wang, X. Jia, L. Li, J. Yang, J. Li, Green Energy Environ. 7 (2022) 307–313.
[31] B.B. Mohammed, K. Yamni, N. Tijani, A.A. Alrashdi, H. Zouihri, Y. Dehmani, I.M. Chung, S.H. Kim, J. Mol. Liq. 296 (2019) 111997.
[32] D.Y. Peng, D.B. Robinson, Ind. Eng. Chem. Fundam. 15 (1976) 59–64.
[33] R.L.C. Akkermans, N.A. Spenley, S.H. Robertson, Mol. Simul. 39 (2013) 1153–1164.
[34] T.F. Willems, C.H. Rycroft, M. Kazi, J.C. Meza, M. Haranczyk, Microporous Mesoporous Mater. 149 (2012) 134–141.
[35] M. Pinheiro, R.L. Martin, C.H. Rycroft, A. Jones, J. Mol. Graph. Model. 44 (2013) 208–219.
[36] Y.F. Hu, K.L. Xue, X.C. Yu, J.X. Hou, J. Polym. Res. 26 (2019) 1–8.
[37] E. Moulin, C.C. Carmona-Vargas, N. Giuseppone, Chem. Soc. Rev. 52 (2023) 7333–7358.
[38] D. Li, K. Panchal, R. Mafi, Macromolecules 51 (2018) 6997–7012.
[39] D. Li, K. Panchal, N.K. Vasudevan, Chem. Eng. Sci. 249 (2022) 117334.
[40] M. Wang, J. Jiang, Adv. Funct. Mater. 34 (2024) 2314683.
[41] Y. Zhang, S.I. Furukawa, T. Nitta, Sep. Purif. Technol. 32 (2003) 215–221.
[42] J.W. Oh, K.Y. Cho, M.Y. Kan, H.J. Yu, D.Y. Kang, J.S. Lee, J. Membr. Sci. 596 (2020) 117735.
[43] G. Qin, A. Du, Q. Sun, Energy Technol. 6 (2018) 205–212.
[44] L. Zhang, Z. Hu, J. Jiang, J. Phys. Chem. C 116 (2012) 19268–19277.
[45] G. Yilmaz, S. Keskin, Ind. Eng. Chem. Res. 51 (2012) 14218–14228.
[46] A.T. Hagler, S. Lifson, P. Dauber, J. Am. Chem. Soc. 101 (1979) 5122–5130.
[47] A. Ozcan, S. Keskin, J. Chem. Technol. Biotechnol. 90 (2015) 1707–1718.
[48] Z. Meng, Q. Li, H. Sun, Y. Wang, X. Li, Green Energy Environ. 10 (2025) 1326–1336.
[49] R. Pan, X. Tu, X. Ma, L. Liu, T. Yan, M. Tong, Chem. Eng. Sci. 310 (2025) 121520.
[50] Y. Qiu, L. Chen, X. Zhang, D. Wang, Y. Tian, Z. Zhou, AIChE J. 70 (2024) e18575.
[51] Y. Qiu, L. Wang, L. Chen, Z. Zhou, J. Wu, Y. Tian, Chem. Sci. 16 (2025) 17450–17460.